Analysis and Design of MMC-Based High-Power DC–DC Converter With Trapezoidal Modulation

Mohd Shadab Ansari, *Student Member, IEEE*, Anshuman Shukla, *Senior Member, IEEE*, and Himanshu J. Bahirat, *Senior Member, IEEE*

***Abstract*—The modular multilevel converter (MMC) based dc–dc converters (MMDCs) are essential for voltage matching, galvanic isolation, renewable integration, and other applications in high voltage direct current systems. The trapezoidal modulation in these converters has been a proven advantage owing to reduced capacitive requirement and high power density. However, the existing short overlap (SO) trapezoidal modulation technique presents significant dc-link current ripples requiring bulky dc-link filter. This article introduces an extended overlap (EO) modulation technique in MMDC to mitigate the need of dc-link filters. The change in overlap angle alters the conduction states, component sizing, harmonic spectrum, and other converter parameters. Therefore, a detailed mathematical analysis of MMDC with both SO and EO modes of trapezoidal modulation is carried out in this article. The effect of change in overlap duration on size of submodule capacitor, dc-link filter is analyzed by simulation and analytical studies. A single-stage three-phase MMC experimental setup is built to verify the converter operation in both SO and EO modulations.**

***Index Terms*—Capacitive energy storage, dc–dc converter, dual-active bridge, high voltage direct current (HVdc) transmission, modular multilevel converter (MMC), multilevel system.**

I. Introduction

THE high voltage direct current (HVdc) systems have become a preferred choice for efficient long-distance power transfer, interconnection of asynchronous ac systems, collecting power from renewables, and remotely located power generation plants [1]. The development of HVdc links over different time and manufacturers for different technical applications resulted into mismatched systems in terms of voltages and technology [2], [3]. The most of existing HVdc systems are of point-to-point type, without a common grid code. The interconnection of these existing point-to-point HVdc links to form a dc grid necessitates voltage matching and power flow control devices. The voltage transformation has always been a crucial aspect of the power systems, which was accomplished by transformers in conventional ac grids. However, power electronic transformers have to be used to achieve the similar objective in the dc grids. Additionally, these power electronic transformers can also control the amount of power transfer. The isolated dc–dc converters consisting of two dc–ac converters connected in front-to-front manner via an intermediate ac transformer are reported in the literature [4], [5], [6]. The galvanic isolation is a desirable feature for grounding flexibility and safety measures. However, these advantages are achieved with additional cost and space engendered by the ac transformer [7]. Thankfully, the dc–dc converters have the liberty to choose operating frequency higher than conventional power frequency (50 or 60 Hz) to minimize the size of the passive components [8].

The modular multilevel converter (MMC) has emerged as the most striking multilevel topology at high voltage levels because of its modularity, scalability, redundancy, high efficiency, better harmonic performance, etc. [9], [10]. However, the conventional ac–dc/dc–ac applications of MMC in HVdc systems operate with sinusoidal modulation, which requires bulky submodule (SM) capacitors due to the large energy storage requirement (ESR) [11]. The isolated MMC-based dc–dc converters contain local ac link, which allows the converter to operate with other modulation techniques also.

The trapezoidal modulation, also called as quasi-two-level modulation, has been proven a superior method compared to the sinusoidal modulation due to the reduced ESR and high power transfer capability [12], [13], [14], [15], [16]. A quasi-two-level operation of MMC along with pulsewidth modulation technique was discussed in [12] to limit the branch energy variation. However, the modularity is lost and it requires high switching frequency, which may not be scalable to high voltage and power application. The quasi-two-level operation of MMC is utilized in [13] and [14] for short overlap (SO) duration. In [14], the arm energy variation is estimated by using output current information. However, an accurate arm current estimation is required in order to accurately estimate arm energy deviation. An accurate arm current estimation is presented in this article to minimize the error in ESR. Similarly, trapezoidal modulation is employed in [15] and [16], for varying dc voltage applications, indicating the growing popularity of trapezoidal modulation. However, all the existing literature on MMC-based dc–dc converters adopt the SO version of trapezoidal modulation [13], [14], [15], [16].

Manuscript received 4 October 2022; revised 22 December 2022; accepted 5 February 2023. Date of publication 27 February 2023; date of current version 20 April 2023. Recommended for publication by Associate Editor Y. Mohamed. This work was supported by the R&D work undertaken in the project under Grants TETRA (TTR/2021/000048) and CRG (CRG/2018/000926) schemes by Science and Engineering Board, Government of India. *(Corresponding author: Anshuman Shukla.)*

The authors are with the Department of Electrical Engineering, Indian Institute of Technology Bombay, Mumbai 400076, India (e-mail: msansari@ee.iitb.ac.in; ashukla@ee.iitb.ac.in; hjbahirat@ee.iitb.ac.in).

Color versions of one or more figures in this article are available at https://doi.org/10.1109/TPEL.2023.3249463.

Digital Object Identifier 10.1109/TPEL.2023.3249463

In the SO version, the time duration of simultaneous conduction of both the arms of a phase leg is less than $60°$, which imposes significant six pulse ripples on the dc side. This necessitates a requirement of bulky dc-link filter arrangement. This large dc-link capacitor may also result in the generation of high discharge current in the event of dc-side faults. Furthermore, the SO modulation imposes higher harmonic components on the ac transformer making transformer design complex [13]. To overcome these issues, this article proposes an extended overlap (EO) operation of MMC-based dc–dc converter. In this proposed method, the overlap duration of arm conduction is more than $60°$, which provides the necessary filtering for the dc-link current and mitigates dc filtering requirement.

Furthermore, this work analyses converter operation in both the SO and EO modes of trapezoidal modulation. The converter operation in trapezoidal method introduces several challenge in terms of converter analysis compared to sinusoidal modulation. The time-varying equivalent states and nonlinear waveforms require thorough mathematical approach for converter analysis and sizing. The major parameters required for converter sizing, such as transformer current, arm current, SM capacitor voltages, dc-link current, power transfer, etc., are derived for different overlap durations. The ESR in both operating modes is derived using analytical studies and verified by simulation studies. The effects of change in overlap angle on power flow, SM and dc-link ESR, converter losses, and ac and dc-side harmonics are analyzed. The existing methods use the phase output current information for sizing the SM capacitors, which results in inaccurate estimation [13], [14]. This article presents a more accurate approach for capacitor size calculation by introducing an arm current estimation method in trapezoidal modulation. The analysis presented in this article lays a basis for analyzing and designing of other converters structures also, which operate with trapezoidal modulation [17], [18], [19], [20].

The rest of this article is organized as follows. The circuit structure, operation of dc–dc converter, and modes of trapezoidal modulation are explained in Section II. The mathematical modeling and sizing of the converter are presented in Section III. The modular-multilevel-based dc–dc converter (MMDC) is simulated with trapezoidal modulation in PSCAD/EMTDC and results are shown in Section IV. The hardware setup and experimental results are discussed in Section V. Finally, Section VI concludes this article. The operation of the converter in both SO and EO modes is validated on a laboratory prototype.

II. Topology and Operation of MMDC

A. Circuit Structure

The dc–dc converter consisting of two MMCs connected in front-to-front manner is shown in Fig. 1. The ac terminals of both the converters are connected via an intermediate ac transformer. At a time, one converter works as an inverter and the other as a rectifier. The structure of each converter is similar to conventional MMC having three phase legs where each phase leg consists of two arms. An arm consists of N series connected half-bridge SMs each with a blocking voltage of $V_{\rm dc}/N$.

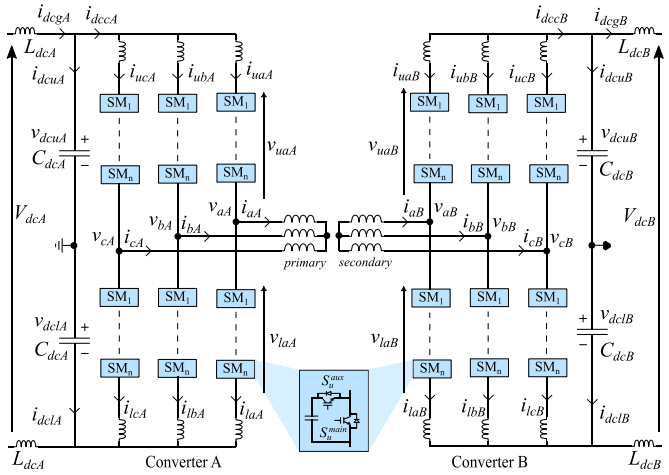

Fig. 1. Circuit diagram of MMDC.

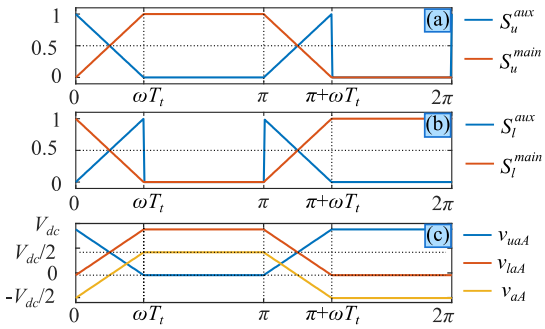

Fig. 2. Switching functions of $S^a_{u,l}$ and main $S^m_{u,l}$ switches of (a) upper, (b) lower arm SMs, and (c) upper, lower, and phase voltage in trapezoidal modulation.

B. Switching Function

There are two switches in a half-bridge SM; auxiliary and main switch, as shown in Fig. 1. There are three possible switching states of a half-bridge SM. The first state is when the auxiliary switch is ON and the main switch is OFF, called as ON state. The second state is when the auxiliary switch is OFF and the main switch is ON, called as OFF state. The third state is when both switches are OFF, called as IDLE state. The switching functions used for trapezoidal modulation are shown in Fig. 2. The auxiliary and main switches of n SMs of an upper arm operate in the complimentary manner except when the output voltage is equal to $\pm V_{\rm dc}/2$ ($V_{\rm dc}$ is used instead of $\pm\ V_{{\rm dc}A}$ to present a general analysis), as during this time, SMs of nonconducting arm remain in IDLE state. The switching functions shown in Fig. 2 can be expressed by (1) and (2) for different time intervals over a fundamental cycle. Similarly, the switching expressions for a lower arm can also be written. The secondary-side converter (converter B) also follows the same switching sequence with a certain phase angle shift (load angle), responsible for the power transfer

$$S_u^{\rm aux}(\theta) = -\frac{\theta}{\omega T_t} + 1 \qquad 0 < \theta < \omega T_t$$
$$= 0 \qquad \omega T_t < \theta < \pi$$

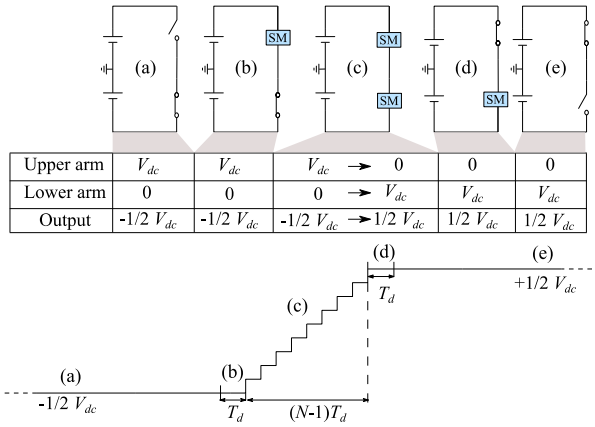

Fig. 3. Phase voltage transition with equivalent circuits.

$$= \frac{\theta - \pi}{\omega T_t} \qquad \pi < \theta < \pi + \omega T_t$$
$$= 0 \qquad \pi + \omega T_t < \theta < 2\pi \tag{1}$$
$$S_u^{\text{main}}(\theta) = 1 - S_u^{\text{aux}}(\theta) \qquad 0 < \theta < \pi + \omega T_t$$
$$= 0 \qquad \pi + \omega T_t < \theta < 2\pi. \tag{2}$$

As observable from the switching functions explained earlier, SM capacitors are inserted only when the output voltage is changing between $V_{\text{dc}}/2$ and $-V_{\text{dc}}/2$. The detailed voltage transition process is explained in the following section.

C. Working Principle

The working principle of a dc–dc converter operated with trapezoidal modulation is similar to the conventional two-level operation, as the ac terminal voltages of converter toggle between positive $(V_{\text{dc}}/2)$ and negative $(-V_{\text{dc}}/2)$ dc bus voltages. However, the difference lies in the transition process between these two voltages. Unlike the two-level converters, the transition is done in multiple intermediate voltage levels (V_{dc}/N) with the help of SMs. The time duration when phase voltage is equal to positive $(V_{\text{dc}}/2)$ dc bus voltage is called positive quasi-state. Similarly, it is called negative quasi-state when output voltage is equal to $(-V_{\text{dc}}/2)$. The duration of phase voltage transition between two consecutive quasi-states is called as transition state $(V_{\text{dc}}/2 \leftrightarrow -V_{\text{dc}}/2)$. The SMs are sequentially inserted or bypassed to provide a smooth transition, during a transition state. The time duration of each intermediate level is called as dwell time (T_d). The minimum limit on the dwell time is governed by allowed dv/dt stress and switch capabilities [13].

The generalized circuit operation while output phase voltage takes transition from negative-to-positive dc bus voltage is explained in Fig. 3 with the help of different equivalent states [see Fig. 3(a) to (e)]. The first equivalent circuit corresponds to the negative quasi-state, as shown in Fig. 3(a). All the upper arm SMs are in IDLE state while the lower arm SMs are OFF during this time. The output phase current is carried by lower arm as upper arm SMs are in IDLE state. The transition process starts from second equivalent circuit when all the upper arm SMs are turned ON and lower arm SMs are still OFF, as shown in Fig. 3(b).

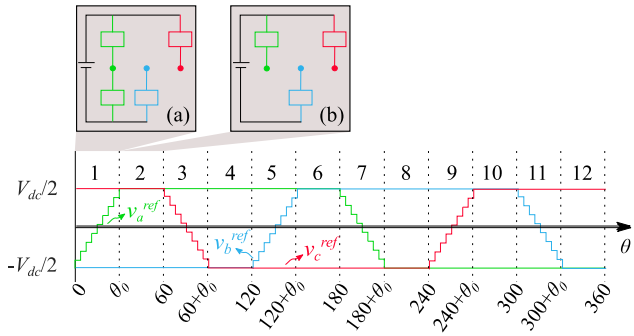

Fig. 4. Different circuit conduction states during SO operation.

The converter operates as per the second equivalent circuit for a duration of dwell time (T_d). After this, upper arm SMs are sequentially tuned OFF while lower arm SMs are sequentially tuned ON, as shown in the third equivalent circuit of Fig. 3(c). The duration for the third equivalent state is $(N-1)T_d$. During this transition, both arms share phase current along with a common mode current, which helps in balancing arm energies. When all the lower arm SMs are turned ON, and all the upper arm SMs are turned OFF, phase voltage reaches positive dc bus voltage. This is shown in the fourth equivalent circuit of Fig. 3(d). This equivalent state remains for a duration of T_d. After this, upper arm SMs still remain OFF while all the lower arm SMs are turned into IDLE state, as shown in the fifth equivalent circuit of Fig. 3(e). In this manner, the output voltage transition completes in $(N+1)T_d$ time.

The SM capacitors conduct current only for this duration of time, which results in low energy deviation in SM capacitors compared to sinusoidal modulation [12]. Moreover, selection of medium operating frequency in ac link further helps in size reduction of SM capacitors and ac transformer and hence, the overall size of converter reduces. The duration of transition state differs for different applications. The trapezoidal modulation can be categorized on the basis of transition duration as SO and EO modes. The detailed circuit behavior of converter for SO and EO modes is analyzed in the following section.

D. Modes of Operation

1) SO Operation: The dc–dc converters used in high-voltage applications operate with trapezoidal modulation instead of square wave modulation to avoid high dv/dt stress. Therefore, the minimum duration of transition state can be chosen such that the dv/dt rate remains within the allowable limits. If the duration of transition state is less than one-sixth of the fundamental time duration, i.e., less than 60^{o}, then it is called SO operation. As illustrated in Fig. 4, from 0^{o} to θ_0^{o} ($\theta_0^{\text{o}} = \omega T_t * 180/\pi$) and 180^{o} to $(180+\theta_0)^{\text{o}}$, phase-*a* operates in transition state. The equivalent circuit of the converter for the first transient state of phase-*a* [i.e., from 0^{o} to θ_0^{o}, shown in Fig. 4(a)] illustrates that both arms of phase-*a* are conducting while in phase-*b* only lower and in phase-*c* only upper arm is conducting. So, in this transition state, dc current has a path to flow through dc link and phase-*a* leg, which is independent of ac side, as shown in Fig. 4(a). However, during θ_0^{o} to 60^{o}, all three phases are in

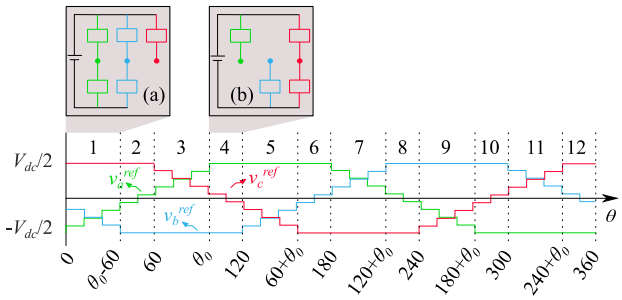

Fig. 5. Different circuit conduction states during EO operation.

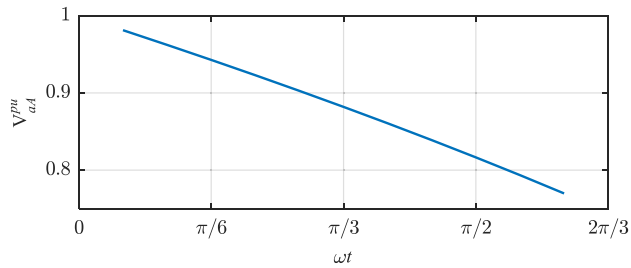

Fig. 6. Per unit rms value of AC trapezoidal voltage.

quasi-state; hence, there is no independent path for dc current to flow, as shown in Fig. 4(b).

Similarly, there are total 12 different intervals of circuit conduction in a fundamental cycle. During six out of 12 intervals (2, 4, 6, 8, 10, 12, see Fig. 4), all phases work in quasi-states. So, there is no independent path for dc-link current during these six intervals. Hence, this results in nonnegligible six pulse ripples in dc-link current and increases dc-side filtering requirement. It is one of the downsides of SO mode operation. Moreover, in the transition state, common mode current flows through the upper and lower arms of a phase, which helps in balancing the arm energies. The short duration of overlap may create challenges in arm energy balancing and current commutation between arms [21]. These issues can be resolved by extending the conduction period of MMC arms, as explained in Section III-B.

2) EO Operation: This mode of operation uses EO duration of the upper and lower arms of a phase leg. In this operation, the duration of transition state is more than one-sixth of fundamental cycle, i.e., more than 60°, as shown in Fig. 5. Similar to the SO operation, EO mode also experiences 12 different conduction intervals over a fundamental cycle. The first interval of transition state of phase-*a* is shown in Fig. 5(a). At this time, phase-*a* and phase-*b* are working in transition state. During the first interval of quasi-state of phase-*a* (interval 4), phase-*c* is working in transition state, as shown in Fig. 5(b).

Similarly, there is always at least one phase leg working in transition state during all the 12 intervals providing circulating path for dc-link current and maintaining dc-link voltage. Hence, in EO mode, the dc-link voltage can be maintained even without dc-side filters. However, to filter out the ripples present in dc-link current, a filter is required but size of this filter is less compared to that in the SO mode of operation. Although, the EO mode requires more energy storage in SMs as the conduction period of SM capacitors is larger than SO mode. The harmonics content in the transformer current in EO mode is less compared to SO mode, which is a desirable feature at very high power levels. The detailed analysis of effect of overlap angle on overall converter sizing is presented in next section.

III. Mathematical Modeling and Sizing of the Converter

The mathematical analysis of MMC operating in the trapezoidal modulation is presented in this section. The waveforms of phase-*a* voltages of converter A (v_{aA}) and referred B (v'_{aB}) are shown in Fig. 6. The time-varying expressions of these voltages with respect to the dc neutral point for a half cycle can be expressed by (3a) and (3b) and the rms values are provided in (4a) and (4b), respectively. The variation in rms value of ac voltage with overlap angle is illustrated in Fig. 6. The ac voltage rms value of EO (70°) is 0.86, which is lower than 0.96 rms value of SO (20°) mode. Nonetheless, it is still higher than 0.707 rms value of sinusoidal modulation, which verifies the higher power transfer capability of trapezoidal modulation than sinusoidal modulation

$$\begin{aligned} v_{aA}(\theta) &= \frac{V_{dcA}}{\omega T_t}\theta - \frac{V_{dcA}}{2} && 0 < \theta < \omega T_t \\ &= \frac{V_{dcA}}{2} && \omega T_t < \theta < \pi \\ &= -\frac{V_{dcA}}{\omega T_t}(\theta - \pi) + \frac{V_{dcA}}{2} && \pi < \theta < \pi + \omega T_t \\ &= -\frac{V_{dcA}}{2} && \pi + \omega T_t < \theta < 2\pi \end{aligned} \tag{3a}$$

$$\begin{aligned} v_{aB}(\theta) &= -\frac{V_{dcB}}{2} && -\pi + \varphi + \omega T_t < \theta < \varphi \\ &= \frac{V_{dcB}}{\omega T_t}(\theta - \varphi) - \frac{V_{dcB}}{2} && \varphi < \theta < \varphi + \omega T_t \\ &= \frac{V_{dcB}}{2} && \varphi + \omega T_t < \theta < \pi + \varphi \\ &= \frac{V_{dcB}}{2} - \frac{V_{dcB}}{\omega T_t}(\theta - \pi - \varphi) && \pi + \varphi < \theta < \pi + \varphi + \omega T_t \end{aligned} \tag{3b}$$

$$V_{aA} = \frac{V_{dcA}}{2}\sqrt{\frac{1}{\pi}\left(\pi - \frac{2\omega T_t}{3}\right)} \tag{4a}$$

$$V_{aB} = \frac{V_{dcB}}{2}\sqrt{\frac{1}{\pi}\left(\pi - \frac{2\omega T_t}{3}\right)}. \tag{4b}$$

A. Transformer Voltage and Current

The dc–dc converter regulates power flow by controlling the phase angle difference (φ) between the ac voltages of the converters. The phase-*a* ac-side voltages measured w.r.t.

TABLE I
ARM CURRENT IN SO MODE

Sr. No.	$v_{aA}(\theta)$	$v_{aB}(\theta)$	$i_{aA}(\theta)$	Time period
1	$\frac{2}{3}\frac{V_{dcA}}{\omega T_t}\theta - \frac{V_{dcA}}{3}$	$-\frac{V_{dcB}}{3}$	$\left(\frac{1}{\omega T_t}\right)\left(\frac{V_{dcA}}{\omega T_t}\frac{\theta^2}{2} - \theta\frac{V_{dcA}-V_{dcB}}{2}\right) + i(0)$	$0 < \theta < \varphi$
2	$\frac{2}{3}\frac{V_{dcA}}{\omega T_t}\theta - \frac{V_{dcA}}{3}$	$\frac{2}{3}\frac{V_{dcB}}{\omega T_t}(\theta-\varphi) - \frac{V_{dcB}}{3}$	$\left(\frac{1}{\omega L_T}\right)\left((\theta^2-\varphi^2)\frac{V_{dcA}-V_{dcB}}{3\omega T_t} - \frac{V_{dcA}-V_{dcB}}{3}(\theta-\varphi) + \frac{2V_{dcB}}{3\omega T_t}\varphi(\theta-\varphi)\right) + i(1)$	$\varphi < \theta < \omega T_t$

TABLE II
ARM ENERGY VARIATION IN SO MODE

Sr. No.	$e^{SO}(\theta)$	Time period
1	$e_{u1}^{SO}(\theta) = \frac{1}{\omega L}\left(-\frac{V_{dcA}^2\theta^5}{15(\omega T_t)^3} + \frac{\theta^4(V_{dcA}^2 - V_{dcA}V_{dcB})}{12(\omega T_t)^2}\right) - \frac{i_0 V_{dcA}\theta^3}{3(\omega T_t)^2} + \frac{1}{\omega L}\left(\frac{V_{dcA}^2\theta^4}{12(\omega T_t)^2} - \frac{\theta^3(V_{dcA}^2 - V_{dcA}V_{dcB})}{9\omega T_t}\right) + \frac{i_0 V_{dcA}\theta^2}{2\omega T_t}$	$0 < \theta < \varphi$
2	$e_{u2}^{SO}(\theta) = \frac{1}{\omega L}(-((\theta^5-\varphi^5)/5 - \varphi^2(\theta^3-\varphi^3)/3)\frac{V_{dcA}^2 - V_{dcA}V_{dcB}}{3(\omega T_t)^3} + \frac{(V_{dcA}^2 - V_{dcA}V_{dcB})((\theta^4-\varphi^4)/4 - \varphi(\theta^3-\varphi^3)/3)}{3(\omega T_t)^2}$ $-\frac{2}{3}\frac{(V_{dcA}V_{dcB})(\varphi(\theta^4-\varphi^4)/4 - \varphi^2(\theta^3-\varphi^3)/3)}{(\omega T_t)^3}) - \frac{i_1 V_{dcA}(\theta^3-\varphi^3)/3}{(\omega T_t)^2} + \frac{1}{\omega L}(((\theta^4-\varphi^4)/4 - \varphi^2(\theta^2-\varphi^2)/2)\frac{V_{dcA}^2 - V_{dcA}V_{dcB}}{3(\omega T_t)^2}$ $-\frac{(V_{dcA}^2 - V_{dcA}V_{dcB})((\theta^3-\varphi^3)/3 - \varphi(\theta^2-\varphi^2)/2)}{3\omega T_t} + \frac{2}{3}\frac{(V_{dcA}V_{dcB})(\varphi(\theta^3-\varphi^3)/3 - \varphi^2(\theta^2-\varphi^2)/2)}{(\omega T_t)^2}) + \frac{i_1 V_{dcA}(\theta^2-\varphi^2)/2}{\omega T_t}$	$\varphi < \theta < \omega T_t$

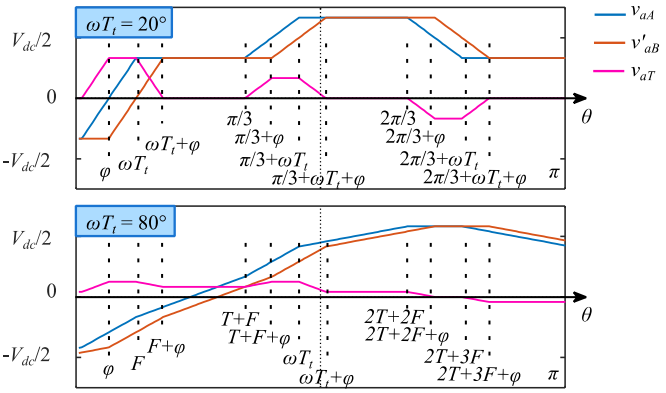

Fig. 7. Primary (v_{aA}), referred secondary v'_{aB}, and equivalent transformer voltages (v_{aT}).

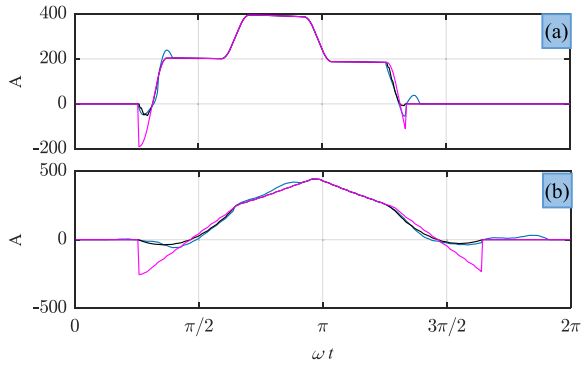

Fig. 8. Actual arm current (blue), existing (pink), and proposed (black) estimated arm current for (a) SO and (b) EO mode of operation.

transformer neutral of primary (v_{aA}) and referred secondary (v'_{aB}) along with the resultant voltage applied across the transformer (v_{aT}) for different overlap angles are shown in Fig. 7. The resultant transformer voltage is equal to the difference between the primary and referred secondary voltages, as given in the following:

$$v_{aT}\ (\theta) = v_{aA}\ (\theta) - v'_{aB}\,(\theta)\,. \tag{5}$$

The transformer current (primary side) can be calculated from transformer voltage, as specified in (6). As transformer resistance is negligibly small, it is neglected while finding the transformer current

$$i_{aA}\ (\theta) = \frac{1}{L_T}\int_0^{\theta} v_{aT}\,(\theta)\,d\,(\theta)\,. \tag{6}$$

The expression of voltage applied across transformer varies across the fundamental cycle and, hence, the transformer current also varies. The transformer current is derived for a half cycle duration for SO and EO modes. There are 12 distinct time intervals in a half cycle, out of which only transient state intervals are listed in Tables I and VI (in the Appendix due to space constraint).

B. Arm Current, Power, and Energy

The phase output currents flow through corresponding upper and lower arms alternatively as one of the arms is disconnected during quasi-states. The upper arms are supposed to conduct during the positive quasi-states and similarly lower arms conduct during the negative quasi-states. Hence, during a transition state, it is expected that complete phase current commutation would take place between the arms. At the time of a transition state, the SM capacitors are inserted in the circuit and the arm current flows through the SM capacitors. Therefore, the arm energy variation takes place during the transition states. The sizing of SM capacitors is done based on the maximum arm energy variation over a fundamental cycle. The arm energy variation can be calculated once the arm current is determined.

For simplicity, in existing the literature, it is assumed that whole phase current is carried by one arm during transition state [12], [14]. However, the actual current carried by the arm differs from the phase current, as shown for a simulated case in Fig. 8. Thereby, this assumption may lead to inaccurate estimation of the ESR in SMs. Additionally, the error in arm energy estimation derived using the existing method increases as the overlap duration increases. To evaluate arm energy variation more accurately, detailed analysis of arm current behavior during

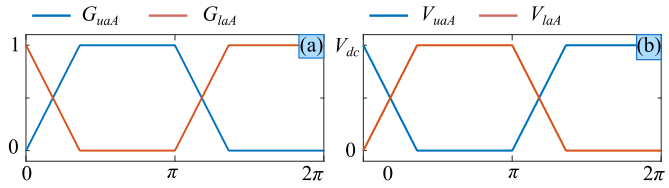

Fig. 9. (a) Factors (G_u) and (G_l) for upper arm and lower arm. (b) Upper and lower arm voltages.

a transition state is carried out. It is observed that the current commutation between arms is almost linear. The outgoing arm current decreases from $i_o(\theta)$ to zero while the incoming arm current increases from zero to $i_o(\theta)$ during transition period (T_t). Following this analysis, the upper (i_{uaA}) and lower (i_{laA}) arm currents of converter-A can be expressed as in (7a) and (7b), respectively. These estimated arm currents are plotted in Fig. 7(a) and (b), it is noticeable that proposed arm estimation provides more accurate estimation compared to existing methods

$$i_{uaA} = G_{uaA}\, i_{aA} \tag{7a}$$

$$i_{laA} = G_{laA}\, i_{aA}. \tag{7b}$$

As observed from (7a) and (7b), the arm currents i_{uaA} and i_{laA} are related with phase current i_{aA} by the factors of G_{uaA} and G_{laA}, respectively. These factors for upper and lower arm currents of phase-a of converter A are expressed as (8a) and (8b), respectively, and plotted in Fig. 9. The similar calculation is valid for other phases also considering the appropriate phase difference

$$\begin{aligned} G_{uaA}\ (\theta) &= \frac{\theta}{\omega T_t} && 0 < \theta\ < \omega T_t \\ &= 1 && \omega T_t < \theta < \pi \\ &= -\frac{\theta - \pi}{\omega T_t} + 1 && \pi < \theta < \pi + \omega T_t \\ &= 0 && \pi + \omega T_t < \theta < 2\pi \end{aligned} \tag{8a}$$

$$\begin{aligned} G_{laA}\ (\theta) &= -\frac{\theta}{\omega T_t} + 1 && 0 < \theta\ < \omega T_t \\ &= 0 && \omega T_t < \theta < \pi \\ &= \frac{\theta - \pi}{\omega T_t} && \pi < \theta < \pi + \omega T_t \\ &= 1 && \pi + \omega T_t < \theta < 2\pi. \end{aligned} \tag{8b}$$

After finding the arm current, the arm power (p_{uaA}) can be calculated by using (9)

$$p_{uaA} = v_{uaA}\, i_{uaA} \tag{9}$$

where (v_{uaA}) is the upper arm voltage of phase-a of converter-A.

The instantaneous arm energy (e_{uaA}) can be obtained from arm power, as given in (10)

$$e_{uaA}\,(\theta) = \int_{\theta_o}^{\theta} p_{uaA}\,(\theta)\, d\,(\theta) + E_{uaA}\,(\theta_o) \tag{10}$$

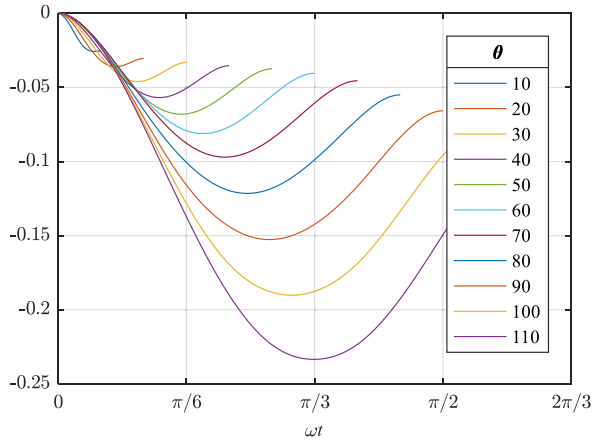

Fig. 10. Arm energy variation (e_{arm}) per unit of power (MW) for different overlap angles.

where $E_{uaA}(\theta_o)$ is initial value of stored energy in arm at θ_o. The instantaneous energy expressions for SO and EO modes are calculated according to (10), as expressed in Tables II and VII (in the Appendix). The variation in arm energy occurs only during transition state of a fundamental cycle. Hence, the arm energy is calculated only for a transition period. If the maxima and minima of arm energy are equal to $\Delta\hat{E}_{uaA}$ and $\Delta\hat{E}_{uaA}$, then the maximum arm energy variation over a fundamental cycle is given by (11)

$$\Delta\, E_{\text{arm}} = \Delta\, E_{uaA} = \Delta\hat{E}_{uaA} - \Delta\breve{E}_{uaA}. \tag{11}$$

The energy variations of the converter with different overlap angles for SO and EO modes of operation are plotted in Fig. 10. It is observable that energy deviation increases with increase in overlap angle as the duration of the arm current conduction through SM capacitors increases with the overlap angle.

C. SM Capacitor Voltage and Sizing

The arm energy deviation obtained in (11) determines the size of SM capacitor. The size of SM capacitor for given arm energy deviation can be calculated using (12) [22]

$$C_{SM} = \frac{\alpha \Delta E_{arm}}{2 N_{SM} V_{SM}^2 \Delta V_{SM}} \tag{12}$$

where N_{SM} is number of SMs in an arm, V_{SM} is the average voltage of an SM, ΔV_{SM} is the allowed per unit ripple in SM capacitor voltage, and α is the safety factor, generally considered as equal to 1.1.

The energy stored in SMs of a single-stage converter (i.e., six arms) can be calculated as follows:

$$E_{SM} = 6 N_{SM} \frac{C_{SM} V_{SM}^2}{2}. \tag{13}$$

The ESR of a converter is generally given in terms of kJ/MVA units. Therefore, the power processed by the converter needs to be calculated. The power processed through one converter

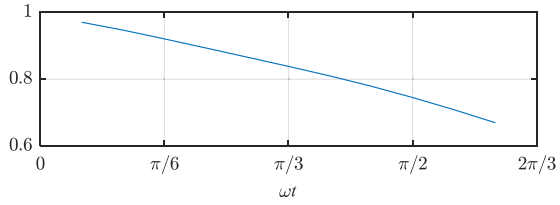

Fig. 11. Per unit power transfer (P_{conv}) variation with overlap angle for a given load angle.

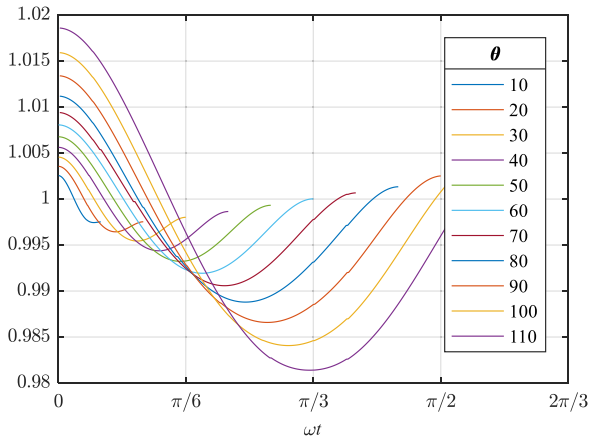

Fig. 12. Per unit SM capacitor voltage ripple variation for different overlap.

can be derived from the output voltage and current expressions, as given in (14) and plotted in Fig. 11. It is observed that as overlap angle increases, the amount of power transferred for same load angle decreases. This is due to the reduction in rms value of the transformer voltages with increase in overlap angle

$$P_{\text{conv}} = \frac{3}{\pi} \int_0^{\pi} v(\theta)\, i(\theta)\, d\theta. \tag{14}$$

The second parameter associated with SMs is the SM capacitor voltage profile, which can be obtained after finding the SM capacitor current. The current flowing through SM capacitors can be derived from the arm currents, as given in (15). The SM capacitor voltage derived from the SM capacitor current is given in (16). The SM capacitor voltages are calculated for both the SO and EO modes for different overlap angles, as shown in Fig. 12. The increase in voltage ripple with the overlap angle is observable from Fig. 12. This is due to the increment in current conduction time of SMs

$$i_{uaA}^{\text{cap}} = (1 - S_{uaA})\, i_{uaA} \tag{15}$$

$$v_{uaA}^{\text{cap}} = \left(\frac{1}{\omega C_{SM}}\right) \int i_{uaA}^{\text{cap}} dt. \tag{16}$$

D. Arm Inductor Selection

The arm inductors are chosen to establish the current commutation between upper and lower arms during an overlap period. The voltage across the arm inductor is defined by the difference of dc-link voltage and sum of inserted SM capacitor

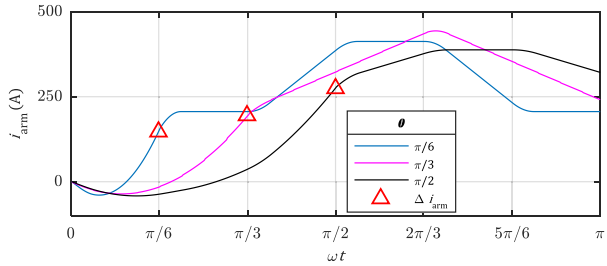

Fig. 13. Arm currents for different overlap angles (triangle markers represent the corresponding Δi_{arm}).

voltages. Therefore, the maximum arm inductor voltage and corresponding maximum arm inductance can be defined by (17) and subsequently by (18)

$$\Delta V_{L_{\text{arm}}}^{\max} = \hat{v}_{dcA} - \Sigma \breve{v}_{SM} = \breve{v}_{dcA} - \Sigma \hat{v}_{SM} \tag{17}$$

$$\Delta V_{L_{\text{arm}}}^{\max} = L_{\text{arm}}^{\max} \frac{\Delta i_{\text{arm}}}{T_t}. \tag{18}$$

The average voltage across the arm inductor ($V_{L_{\text{arm}}}$) across overlap duration is less than the maximum voltage defined in (18), therefore an appropriate arm inductor size can be selected as

$$L_{\text{arm}} < \Delta V_{L_{\text{arm}}}^{\max} \frac{T_t}{\Delta i_{\text{arm}}}. \tag{19}$$

It is noticeable from (19) that the arm inductance value is proportional to overlap duration (T_t) and inversely proportional to Δi_{arm}. Here, Δi_{arm} is the change in arm current value occurring across the overlap duration. The arm current values plotted in Fig. 13 illustrate that the value of Δi_{arm} does not increase in proportion to the overlap angle. Therefore, the required size of arm inductor (L_{arm}) increases with overlap angle. Hence, different size of arm inductors is required for SO and EO modulations.

E. DC-Link Capacitor Sizing

The dc-link capacitor can be sized once the current flowing through dc-link capacitor is obtained. The positive dc pole current at the converter side (i_{dccA}) is the sum of three upper arm currents, as given in (20a). This current contains ripples riding on the dc mean value. The dc-link capacitor is assumed to bypass all these ripples. Hence, it is assumed that dc-link current at the grid side (i_{dcgA}) is the mean value of dc current at the converter side (i_{dccA}) and all the ripples (i_{dcuA}) are by passed to the dc-link capacitor, as given in (20b). angles

$$i_{dccA} = i_{uaA} + i_{ubA} + i_{ucA} \tag{20a}$$

$$i_{dcuA} = i_{dcgA} - i_{dccA}. \tag{20b}$$

The positive dc pole current (i_{dccA}) is plotted for different overlap angles in Fig. 14. The energy associated with the dc-link capacitor can be calculated using (21)

$$e_{dcu}(t) = \int i_{dcu} v_{dcu}\, dt. \tag{21}$$

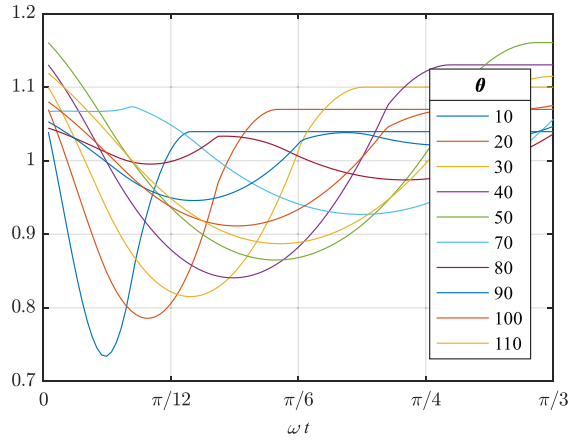

Fig. 14. Per unit DC-link current at the converter side (i_{dccA}) for different overlap angles.

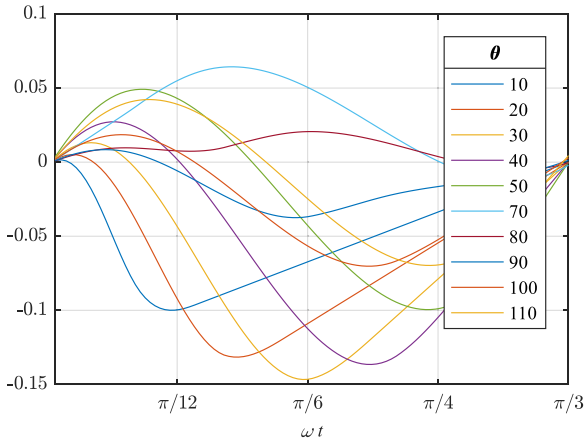

Fig. 15. DC-link energy deviation (E_{dc}) per unit of power (MW) for different overlap angles.

The dc-link capacitor can be sized after finding the energy deviation (ΔE_{dcu}), as given in (22)

$$C_{dcu} = \frac{\beta \Delta E_{dcu}}{2V_{dcu}^2 \Delta V_{dcu}}. \tag{22}$$

Here, V_{dcu} is the upper dc-link capacitor voltage, ΔV_{dcu} is the p.u. voltage ripple, and β is the safety factor. The dc-link capacitor is approximated by assuming that it absorbs all the dc-link current ripples, as mentioned in (20b). The dc-link current is determined from the approximated arm currents, as given in (20a). To account for practical operating conditions, it is observed that a safety factor of 1.5 is a good approximation for both SO and EO modes.

Similar to (13), the energy stored in dc-link capacitor can be calculated as per (23). The total dc-link energy is sum of the energy stored in upper and lower dc-link capacitor, as given in (24). The energy deviations of dc-link capacitor for SO and EO modes are shown in Fig. 15

$$E_{dcu} = \frac{C_{dcu} V_{dcu}^2}{2} \tag{23}$$

$$E_{dc} = E_{dcu} + E_{dcl}. \tag{24}$$

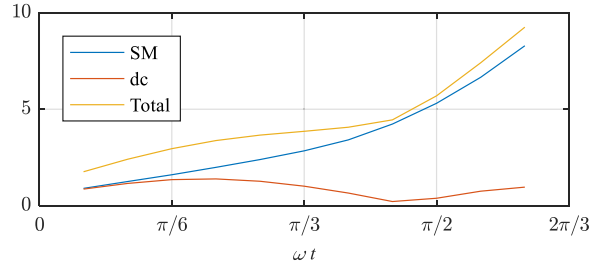

Fig. 16. SM, DC, and total ESR per unit of power transfer (kJ/MVA).

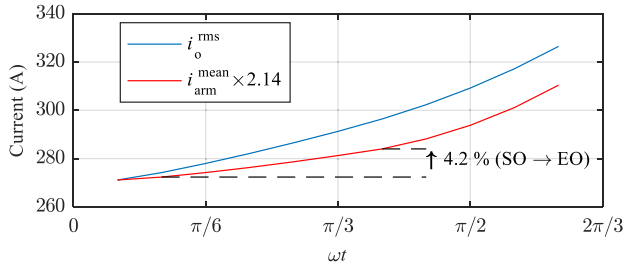

Fig. 17. RMS value of transformer current and mean value of arm current with respect to overlap angle (ωT_t).

The ESR per unit of power transferred, for SMs (E_{SM}/P_{conv}) and dc link (E_{dc}/P_{conv}), is calculated using (13) and (24) and plotted for different overlap angles, as shown in Fig. 16. The values plotted in Fig. 16 are calculated for a fundamental frequency of 250 Hz and voltage ripple of $\pm 1\%$. The ESR in SMs increases with the increment in overlap angle because the SMs conduct the arm current for a longer time duration. On the other side, the ESR at dc side does not change in linear manner with overlap angle. The ESR at the dc side can be understood by the wave shape of dc-link current shown in Fig. 14. The ripple in dc-link current depends on the magnitude and duration of dc current ripple. The minimum ESR at dc side occurs near 70°–80° of overlap angle, as illustrated in Fig. 16. However, the total ESR increases with the increment in overlap angle as the major energy requirement lies in SMs.

The dc–dc specific applications require limited range of power factor [12], [14]. Hence, it is found that the ESR of MMDC with sinusoidal modulation is approximately equal to 22 kJ/MVA. It is noticeable from Fig. 16 that the total ESRs of SO and EO modes are much lesser than the sinusoidal modulation. Although, the SM capacitor size is more in EO mode, the dc current ripples and, hence, the size of dc-link capacitors is less than SO mode. Thus, the EO modulation could be useful in the applications where bulky dc-link capacitor is not desired to limit the fault feed during dc-side faults.

F. Converter Loss Estimation

The converter ac voltages in the EO modulation contain less harmonics content than SO modulation, as also apparent from Fig. 17 . Therefore, the EO modulation employs comparatively higher transformer rms current than SO modulation for a given transferred power. Accordingly, the arm current and, hence, the

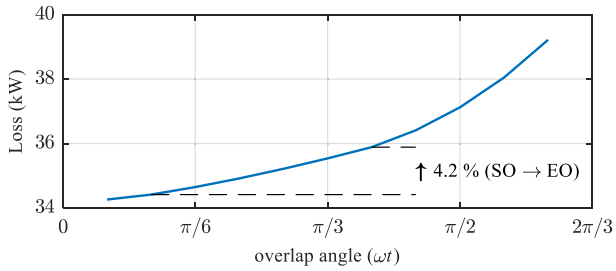

Fig. 18. Converter losses for different values of overlap angle.

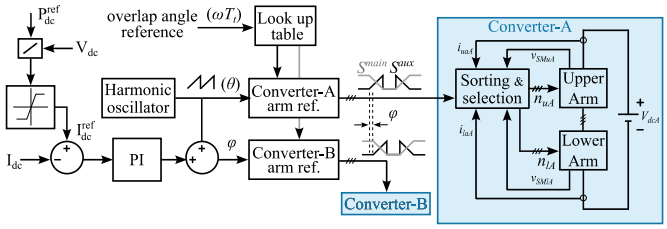

Fig. 19. Block diagram of MMDC control with trapezoidal modulation.

conduction losses also vary with a change in overlap angle. The following analysis is carried out to explicate the dependence of converter currents and losses on the value of overlap angle.

The losses occurring in the converter switches are governed by the current carried by the switching devices, as given in (25)

$$P_{\text{loss}} = \frac{6}{2\pi} \int_0^{2\pi} N_{SM} V_f i_{uaA} d\theta \tag{25}$$

where N_{SM} is the number of SMs in an arm, V_f is the forward voltage drop across a switch, and i_{uaA} is the upper arm current of phase-a. N_{SM} and V_f are decided at the design stage based on the converter application. It is evident from (25) that the conduction losses of the converter depend on the average/mean value of the arm current, which itself depends on the overlap angle value, as illustrated in Fig. 17. The rms value of the transformer current is also plotted in Fig. 17 for a comparison purpose. It is noticeable that the increment in the mean value of arm current is less than the increment in the rms value of transformer current for a constant power throughput. An increment of 4.2% in the mean value of arm current was observed from SO to EO modulation, as shown in Fig. 17. Thus, the losses presented in (25) also increase by 4.2% in EO modulation compared to the SO modulation.

The losses occurring in the MMDC for the simulation case presented in the manuscript ($P_{\text{conv}} = 15$ MW) are analyzed by using (25) and plotted in Fig. 18. It is observed from Fig. 18 that the converter loss increases with an increment in overlap angle, which is consistent with the aforementioned explanation. However, it is also noticeable that the increment in the conduction losses in EO mode is not very significant.

IV. Simulation Results

The MMDC operated with trapezoidal modulation is simulated to validate the working principle of converter in SO and EO modulation schemes. The circuit diagram of simulated system is shown in Fig. 1. The simulations are done in PSCAD/EMTDC.

TABLE III
Simulation Parameters for SO

Parameters	Primary	Secondary
DC voltage (V_{dc})	40 kV	60 kV
DC inductor (L_{DC})	0.0015 H	0.0015 H
DC capacitor (C_{DC})	75 μF	75 μF
DC resistance (R_{DC})	50 mΩ	
No of SMs (N) per arm	10	
SM capacitance C_{SM}	100 μF	
Arm inductance (L_{arm})	50 μH	20 μH
Arm resistance (R_{arm})	80 mΩ	
Operating frequency	250 Hz	
Transformer ratio (n_T)	40 kV /60 kV	

TABLE IV
Simulation Parameters for EO

Parameters	Primary	Secondary
DC voltage (V_{dc})	40 kV	60 kV
DC inductor (L_{DC})	0.0015 H	0.0015 H
DC capacitor (C_{DC})	NA	NA
DC resistance (R_{DC})	50 mΩ	
No of SMs (N) per arm	10	
SM capacitance C_{SM}	300 μF	
Arm inductance (L_{arm})	170 μH	60 μH
Arm resistance (R_{arm})	80 mΩ	
Operating frequency	250 Hz	
Transformer ratio (n_T)	40 kV /60 kV	

The circuit consists of two MMCs connected in front-to-front manner with an ac transformer in intermediate ac link. The dc sides of MMCs are connected to their respective dc sources. The internal ac stage is represented by an ac transformer with 10% impedance. The SMs are utilized to achieve smooth transition in output voltage from one dc pole voltage to another.

An overview of converter control is explained by the block diagram shown in Fig. 19. A harmonic oscillator is used to generate the reference angle (θ) since there is no ac grid reference available for the dc–dc converters. This reference angle is directly sent to the arm reference generation blocks of converter-A. The reference angle of converter-B is generated using a power controller similar to the control scheme discussed in [13]. The power controller calculates the dc-link current reference using the reference power and respective dc-link voltage, followed by a rate of change limiter. A look table is produced based on the required overlap angle value (ωT_t). The arm reference generator blocks use these look tables and generate the switching functions of the arms. These switching functions are used by the sorting and selection program to produce the final insertion indices of upper (n_{uA}) and lower (n_{uB}) arms of converter-A and converter-B. The simulation result employing these control steps for trapezoidal modulation is discussed below.

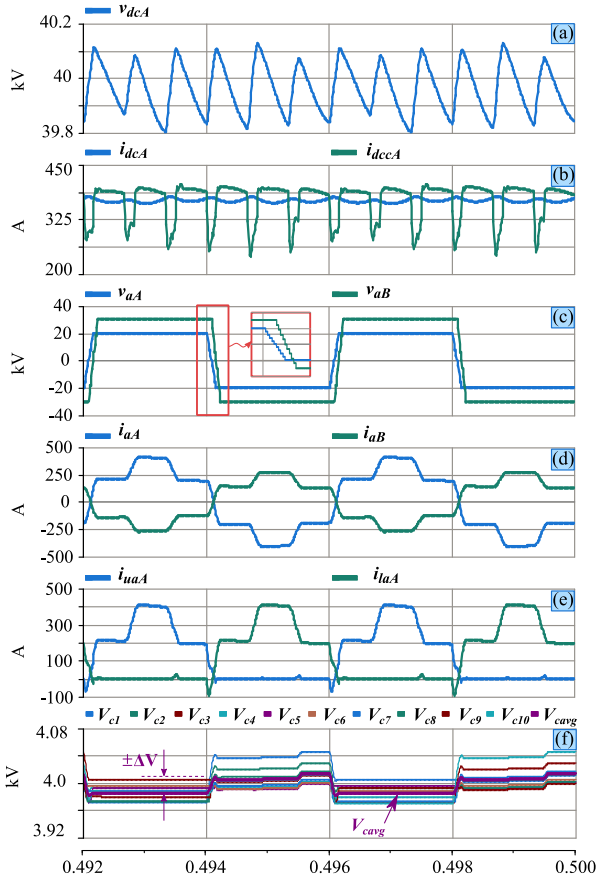

Fig. 20. Simulation results in SO mode of operation: (a) DC-link voltage, (b) DC-link currents, (c) phase voltages, (d) phase currents, (e) arm currents, and (f) SM capacitor voltages.

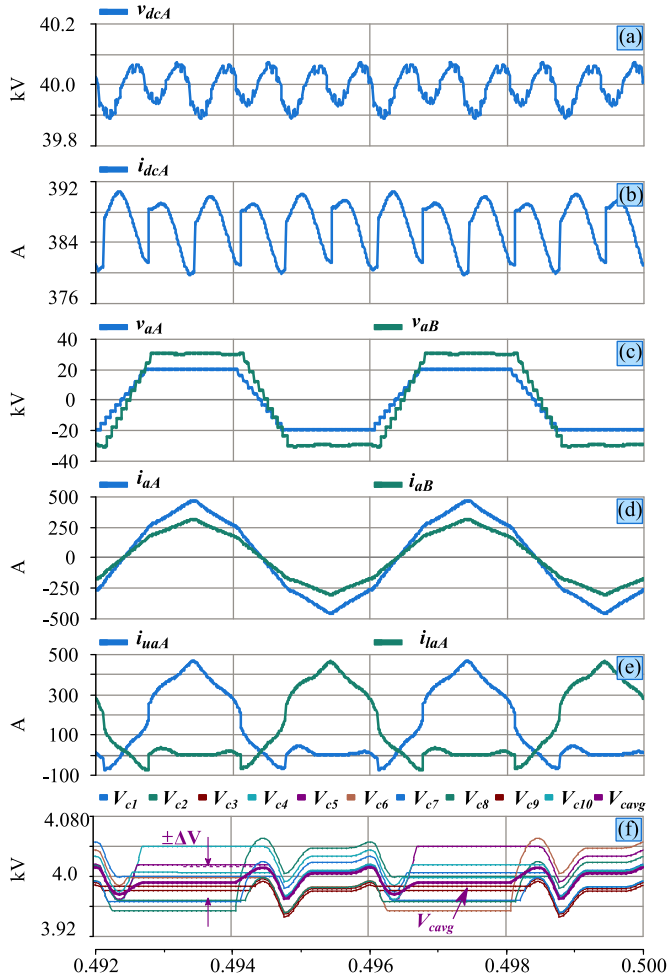

Fig. 21. Simulation results in EO mode of operation: (a) DC-link voltage, (b) DC-link current, (c) phase voltages, (d) phase currents, (e) arm currents, and (f) SM capacitor voltages.

A. SO Mode

The MMDC working in SO mode is simulated in this section. The simulation parameters are listed in Table III. The simulation results are shown in Fig. 20. The dc-link voltage measured before dc filter contains $6n$ ripples, as shown in Fig. 20(a). Similarly, the dc-link currents before (I_{dcA}) and after the dc-link filter (I_{dccA}) are illustrated in Fig. 20(b). Apparently, the ripples present in I_{dccA} are significant, which require dedicated filtering. The ripple in filtered dc-link current is maintained well within the limit by using dc-side filters. The voltages of both the dc links are almost ripple free, as shown in Fig. 20(a). Similarly, the dc-link currents are also constant, as shown in Fig. 20(b). The ripple in dc-link voltages and currents is maintained well within the limit by using the dc-side filters. The trapezoidal output voltages of phase-a of both the converters measured with respect to the midpoint of respective dc link are shown in Fig. 20(c). The power is getting transferred from converter A to B and the required phase difference between these voltages (φ) is determined using (14).

It is observed from the phase voltage waveforms that transition between two quasi-states is done with a controlled slope. The transition or overlap duration is chosen at 15 ° (less than 60°) as it is the SO mode operation. The output currents of phase-a of both the converters are shown in Fig. 20(d). The upper and lower arm currents of phase-a of converter-A are shown in Fig. 20(e). The wave shape of arm currents is consistent with the analysis presented in the previous section. The reduced switching sorting and selection method are used for less computational burden and faster simulation. In this method, the SMs are sorted and selected only when there is a change in output level rather than at every sample period. The SM capacitor voltages of upper arm of phase-a of primary converter are shown in Fig. 20(f). It is observed that the SM capacitor voltages are very well maintained around their mean value. The calculated and simulated peak-to-peak SM voltage ripple is around 0.6%, which validates the accuracy of the analysis presented in this article.

B. EO Mode

The dc–dc converter structure is simulated in the EO mode with the parameters given in Table IV. In the EO mode, the overlap duration could be chosen as any value greater than 60°. Therefore, the overlap duration for the simulation is kept at 70°, where dc-link ripples are low. The simulation results are presented in Fig. 21. The converter is operated without dc-link filter and it is noticeable that the dc-link voltage and current

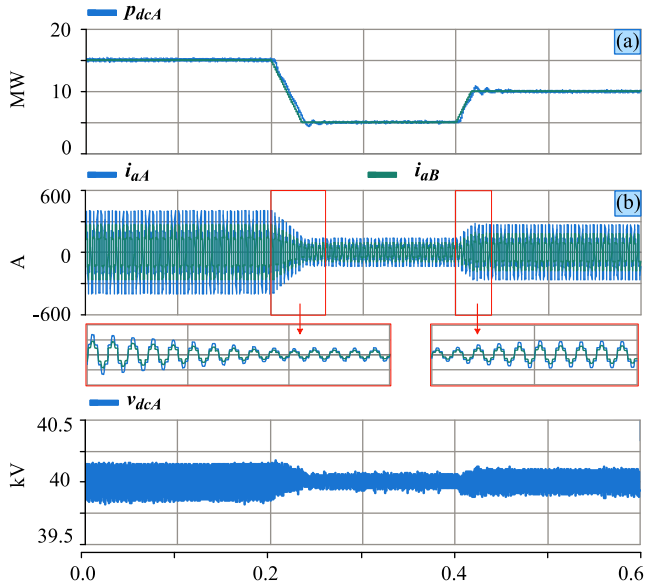

Fig. 22. Simulation results in SO mode of operation: (a) DC-link power, (b) phase currents, and (c) SM capacitor voltages.

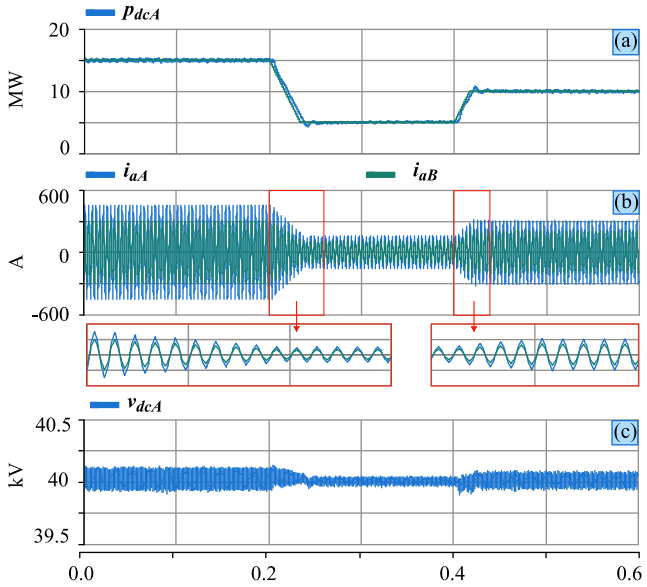

Fig. 23. Simulation results in EO mode of operation: (a) DC-link power, (b) phase currents, and (c) SM capacitor voltages.

are maintained constant, as shown in Fig. 21(a) and (b). Thus, the analysis presented in previous section regarding low dc-link ripple in EO mode is verified with simulation results. The phase-a voltages of both the converters with respect to their dc-link neutral are shown in Fig. 21(c). The phase difference between these voltages is determined using (14), to transfer 15 MW of power. The extended duration of overlap can be observed from the phase voltage waveforms.

The phase-a output current is shown in Fig. 21(d). The wave shape of currents tends more toward sinusoidal shape as compared to SO mode. This is due to the decrement in harmonic components in phase voltages, as harmonics decrease with increase in overlap angle. The upper and lower arm currents are shown in Fig. 21(e). The SM capacitor voltages are shown in Fig. 21(f), which are balanced by reduced switching sorting method. The calculated and simulated SM voltage ripples are around 0.6% and 0.7% of average value, which validates the accuracy of presented analysis.

C. Closed-Loop Control of SO and EO Modes

The closed-loop control illustrated in Fig. 19 is implemented for both the simulation cases of SO and EO modes. The results obtained for the SO modulation case are illustrated in Fig. 22. Three different power set points are tested in the simulation run. Initially, the converter is transmitting 15 MW of power, as shown in Fig. 22(a). The first transition is exercised at 0.2 s by reducing the power set point from 15 to 5 MW. The second transition is exercised at 0.4 s by again ramping up the power transfer from 5 to 10 MW. The phase currents and their zoomed views illustrating the current envelope during transition periods are illustrated in Fig. 22(b). The dc-link voltages are held constant during both the transitions with the help of dc-link capacitors. The similar transition studies as of the SO mode are employed for the EO mode as well, and the results are presented in Fig. 23. It is conspicuous from Fig. 23 that the converter effectively follows the reference power command. The dc-link voltage ripple depends proportionally on the converter's power throughput. However, it is well maintained around the mean value throughout the simulation run without using the dc-link capacitors, as evident from Fig. 23(c).

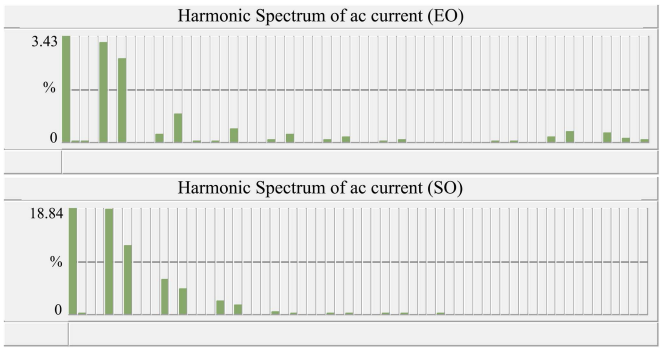

Fig. 24. Percentage harmonic spectrum of transformer/AC current (I_{aA}) normalized against the fundamental component in EO and SO operations.

D. Harmonic Analysis and Comparison

The total harmonic distortion (THD) and harmonic spectrum analysis of the transformer current are carried out to compare the harmonics content of SO and EO modes. It was observed that the harmonic content imposed on the transformer voltage decreases with increment in overlap angle. This phenomenon is noticeable from the harmonic spectrum of transformer current presented in Fig. 24. The THD of phase current in SO mode is approximately equal to 24%, which is significantly higher than the typical ac gird-tied applications. On the other hand, the THD of the phase current in EO mode is equal to 4.3%, which is

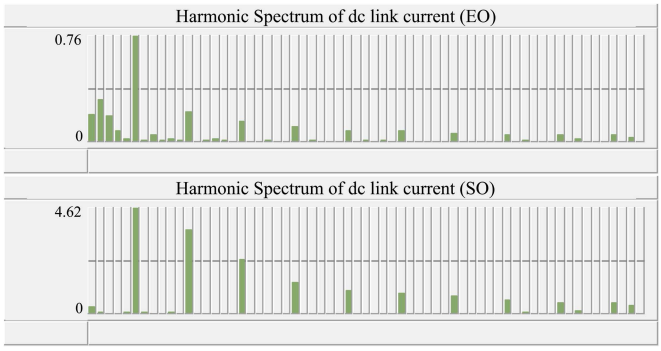

Fig. 25. Percentage harmonic spectrum of DC-link current normalized against the average/DC component in EO and SO operations.

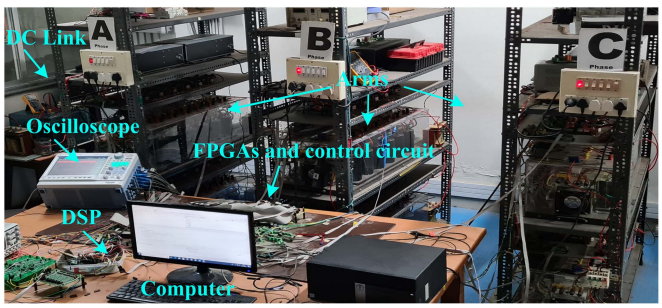

Fig. 26. Three-phase MMC hardware setup.

TABLE V
HARDWARE PARAMETERS

Parameters	Value
DC voltage (V_{DC})	200 V
No of SMs per arm	6
SM capacitance	2.2 mF
No. of output levels	7
Transformer ratio	1:1.33
Operating frequency	50 Hz
Load impedance	50/100 Ω

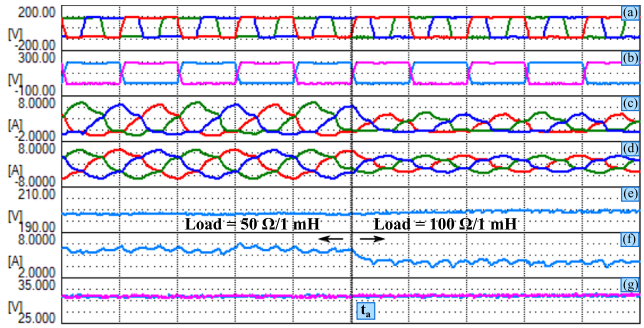

Fig. 27. Hardware results for step load change (50 to 100 Ω) in SO mode of operation: (a) Output voltages, (b) upper and lower arm voltages of phase-*a*, (c) upper arm currents, (d) output currents, (e) DC-link voltage, (f) DC-link current, and (g) SM capacitor voltages. Time base is 2 ms/div.

of the similar order as of sinusoidal modulation. Therefore, the conventional coupling transformer design used for the sinusoidal modulation could also be adopted for the MMC operated with EO modulation scheme, which may not be consistent with the SO mode.

The harmonic spectrum of the dc-link current without dc-side filter is also studied and the results are presented in Fig. 25 . This study is carried out to substantiate the need of dc-link filter in SO mode and to support the analysis presented in Section II-D. It is apparent that the magnitudes of harmonics content present in SO modulation are higher compared to the EO modulation. In the EO modulation, at least one of the phase-legs works in the transition state, providing the filtering path for the dc-link current. On the other hand, in SO modulation, six out of total 12 conduction states has no phase-leg working in a transition state, as illustrated in Figs. 4 and 5. Therefore, during these states, the dc-link current has no independent path and has to flow through the ac side resulting in significant dc-link ripples. Likewise, in the SO modulation, the ac voltages and currents of the converter contain more harmonics content than EO modulation. Consequently, these harmonics content reflect at the dc side as well, resulting in a polluted dc-link current profile. It is observed that the EO modulation experiences around 3.6% ripple in the dc-link current. This small amount of ripple can be filtered by the dc transmission lines or by using small dc-link capacitors. However, in the SO modulation, the dc-link current experiences a significant ripple amount of 28%. Apparently, dedicated dc-link filter is required to filter out these ripples and to maintain a constant dc-link current profile flowing through the transmission line.

V. EXPERIMENTAL VERIFICATION

A three-phase seven-level laboratory prototype of MMC is built to verify the operation of MMC with both SO and EO modes of trapezoidal modulation for different loading conditions. The developed prototype is shown in Fig. 26 and key parameters are listed in Table V. The three-phase setup is controlled by a master controller and three dedicated slave controllers, one for each phase. The TMS320F28335 digital signal controller is used as a master controller while three separate field-programmable gate arrays are used to implement sorting control for three phases.

The hardware results obtained for the SO mode of operation are shown in Fig. 27. The seven-level output voltages with 15 ° overlap angle are shown in Fig. 27(a). The seven-level trapezoidal upper and lower arm voltages are presented in Fig. 27(b). The three-phase arm and output currents with different loading conditions are shown in Fig. 27(c) and (d). The output and arm current envelops follow a similar wave shape, as illustrated in simulation results. The dc-link voltage and current are shown in Fig. 27(e) and (f). As the load changes from 50 to 100 Ω at a time instance t_a, the magnitudes of all converter currents decrease. The dc-link current contains six pulse ripples due to the trapezoidal modulation, as shown in Fig. 27(f). An arbitrary upper and lower arm capacitor voltages are shown in Fig. 27(g), which are balanced by sorting and

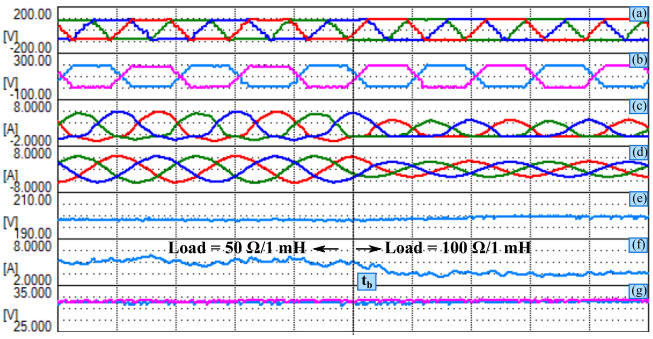

Fig. 28. Hardware results for step load change (50 to 100 Ω) in EO mode of operation: (a) Output voltages, (b) upper and lower arm voltages of phase-*a*, (c) upper arm currents, (d) output currents, (e) DC-link voltage, (f) DC-link current, and (g) SM capacitor voltages. Time base is 2 ms/div.

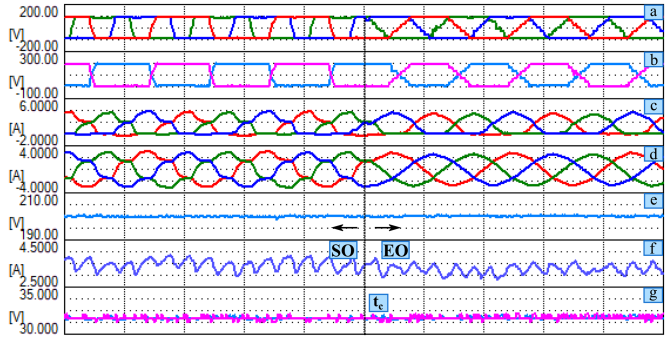

Fig. 29. Hardware results during transition from SO to EO mode: (a) Output voltages, (b) upper and lower arm voltages of phase-*a*, (c) upper arm currents, (d) output currents, (e) DC-link voltage, (f) DC-link current, and (g) SM capacitor voltages. Time base is 2 ms/div.

selection technique. Here, the capacitors used in the setup are obtained from off-the-shelf SM stacks, which are oversized. The experiment is conducted to verify the basic operating principal of converter in trapezoidal modulation and the obtained results match with the simulation and analysis presented in this article.

The developed hardware prototype is also tested for the EO mode of operation with different loading conditions and the results are presented in Fig. 28. The three-phase output voltages, upper and lower arm voltages are shown in Fig. 28(a) and (b), respectively. The overlap angle for the trapezoidal modulation is selected as 70°. The harmonic components present in output voltages are less compared to that in the SO mode. The upper and lower arm currents of phase-*a* are shown in Fig. 28(c) and three-phase output currents shown in Fig. 28(d). The ac currents are further smoothened by the coupling transformer. Hence, the harmonic components carried by the transformer are less compared to that in the SO mode. The loading of the converter is changed at time instance t_b, the change in magnitude of output current and arm currents can be noticed in Fig. 28(c) and (d). The dc-link voltage and current are shown in Fig. 28(e) and (f). The SM capacitor voltages of an upper and lower arm of phase-*a* are plotted in Fig. 28(g). Here, the basic experimental studies were conducted to observe the converter operation for different overlap angles and the results presented in Figs. 27 and 28 verify the satisfactory operation of the converter for both SO and EO modes with different loading conditions.

The hardware results presented in Fig. 29 illustrate the transient operation of MMC from SO to EO mode by changing the overlap angle from 15° to 70° at a time instant t_c. The change in overlap angle is observable in the three-phase output voltages and arm voltages, as shown in Fig. 29(a). As discussed earlier, the harmonic components in the output voltage decrease with increment in overlap angle, which is also replicated in arm and output currents, as shown in Fig. 29(c) and (d). The output current is carried by the upper arm in the positive half cycle and by the lower arm in the negative half cycle, as explained earlier in the working principle of the converter operation. The dc-link voltage and current are shown in Fig. 29(e) and (f). The dc-link current ripple decreases slightly in EO mode compared to SO mode, as shown in Fig. 29(f). The balanced SM capacitor voltages are illustrated in Fig. 29(g). Thus, it can be concluded that the presented experimental results validate the converter operation in both the SO and EO trapezoidal modulation. It was observed that the harmonic content in ac currents and dc-link current reduces in EO mode. Finally, all the experimental wave shapes are in decent accord with the simulation and analytical results.

VI. Conclusion

The MMC working with trapezoidal modulation was analyzed and discussed in this article. The converter behavior in SO and EO modes of operation was explained. A generalized mathematical analysis considering the trapezoidal modulation was presented. An arm current estimation is presented to accurately derive the arm energy deviation. The key converter parameters, such as transformer current, arm current, power flow, and SM capacitor voltage, were derived and illustrated for different operating conditions. The trapezoidal modulation of multilevel converters is finding application in other converter structures also and hence, the analysis presented in this work can also be adopted for other converters. The operation in trapezoidal modulation reduces the energy storage burden on the SM capacitors compared to that with the sinusoidal modulation. However, this is achieved at a cost of additional dc-link filter. The distribution of ESR between SMs and the dc-link filter varies with the change in overlap angle. The estimation of ESR in SMs and dc-link capacitor for different overlap angles was derived in this work. The mitigation of dc-link filter by the proposed EO mode was analyzed and verified by simulation results. The simulation studies of MMC-based dc–dc converter, including harmonic analysis, were presented, which are in agreement with the proposed mathematical analysis. An experimental setup was also developed and the operation of MMC with both the SO and EO modes was verified.

Appendix

See Tables VI and VII.

TABLE VI
ARM CURRENT IN EO MODE

Sr. No.	$v_{aA}(\theta)$	$v_{aB}(\theta)$	$i_{aA}(\theta)$	Time period
1	$\frac{V_{dcA}}{\omega T_t}\theta-\frac{V_{dcA}}{2}-\frac{1}{3}\left(\frac{V_{dcA}}{\omega T_t}F-\frac{V_{dcA}}{2}\right)$	$-\frac{V_{dcB}}{2}-\frac{1}{3}\left(-\frac{V_{dcB}}{\omega T_t}(\theta+T+F-\varphi)+\frac{V_{dcB}}{2}\right)$	$\left(\frac{1}{\omega L}\right)\left(\frac{3V_{dcA}-V_{dcB}}{3\omega T_t}\frac{\theta^2}{2}-\frac{V_{dcA}F+V_{dcB}(T+F-\varphi)}{3\omega T_t}\theta-\frac{(V_{dcA}-2V_{dcB})}{3}\theta\right)+i_0$	$0<\theta<\varphi$
2	$\frac{V_{dcA}}{\omega T_t}\theta-\frac{V_{dcA}}{2}-\frac{1}{3}\left(\frac{V_{dcA}}{\omega T_t}F-\frac{V_{dcA}}{2}\right)$	$\frac{V_{dcB}}{\omega T_t}(\theta-\varphi)-\frac{V_{dcB}}{2}-\frac{1}{3}\left(\frac{V_{dcB}}{\omega T_t}F-\frac{V_{dcB}}{2}\right)$	$\left(\frac{1}{\omega L}\right)\left(\frac{V_{dcA}-V_{dcB}}{\omega T_t}\frac{\theta^2-\varphi^2}{2}-\frac{V_{dcA}F-V_{dcB}(F+3\phi)}{3\omega T_t}(\theta-\phi)-\frac{(V_{dcA}-V_{dcB})}{3}(\theta-\phi)\right)+i_1$	$\varphi<\theta<F$
3	$\frac{V_{dcA}}{\omega T_t}\theta-\frac{V_{dcA}}{2}-\frac{1}{3}\left(\frac{V_{dcA}}{\omega T_t}\theta-\frac{V_{dcA}}{2}\right)$	$\frac{V_{dcB}}{\omega T_t}(\theta-\varphi)-\frac{V_{dcB}}{2}-\frac{1}{3}\left(\frac{V_{dcB}}{\omega T_t}F-\frac{V_{dcB}}{2}\right)$	$\left(\frac{1}{\omega L}\right)\left(\frac{2/3V_{dcA}-V_{dcB}}{\omega T_t}\frac{(\theta^2-F^2)}{2}+\frac{V_{dcB}}{3\omega T_t}(F+3\varphi)(\theta-F)-\frac{V_{dcA}-V_{dcB}}{3}(\theta-F)\right)+i_2$	$F<\theta<F+\varphi$
4	$\frac{V_{dcA}}{\omega T_t}\theta-\frac{V_{dcA}}{2}-\frac{1}{3}\left(\frac{V_{dcA}}{\omega T_t}\theta-\frac{V_{dcA}}{2}\right)$	$\frac{V_{dcB}}{\omega T_t}(\theta-\varphi)-\frac{V_{dcB}}{2}-\frac{1}{3}\left(\frac{V_{dcB}}{\omega T_t}(\theta-\varphi)-\frac{V_{dcB}}{2}\right)$	$\left(\frac{1}{\omega L}\right)\left(\frac{2}{3}\frac{V_{dcA}-V_{dcB}}{\omega T_t}\frac{(\theta^2-(F+\varphi)^2)}{2}+\frac{2}{3}\frac{V_{dcB}}{\omega T_t}\varphi(\theta-F-\varphi)-\frac{V_{dcA}-V_{dcB}}{3}(\theta-F-\varphi)\right)+i_3$	$F+\varphi<\theta<T+F$
5	$\frac{V_{dcA}}{\omega T_t}\theta-\frac{V_{dcA}}{2}-\frac{1}{3}\left(\frac{V_{dcA}}{\omega T_t}(T+F)-\frac{V_{dcA}}{2}\right)$	$\frac{V_{dcB}}{\omega T_t}(\theta-\varphi)-\frac{V_{dcB}}{2}-\frac{1}{3}\left(\frac{V_{dcB}}{\omega T_t}(\theta-\varphi)-\frac{V_{dcB}}{2}\right)$	$\left(\frac{1}{\omega L}\right)\left(\frac{V_{dcA}-2/3V_{dcB}}{\omega T_t}\frac{(\theta^2-(T+F)^2)}{2}-\frac{V_{dcA}(T+F)-V_{dcB}(2\varphi)}{3\omega T_t}(\theta-T-F)-\frac{V_{dcA}-V_{dcB}}{3}(\theta-T-F)\right)+i_4$	$T+F<\theta<T+F+\varphi$
6	$\frac{V_{dcA}}{\omega T_t}\theta-\frac{V_{dcA}}{2}-\frac{1}{3}\left(\frac{V_{dcA}}{\omega T_t}(T+F)-\frac{V_{dcA}}{2}\right)$	$\frac{V_{dcB}}{\omega T_t}(\theta-\varphi)-\frac{V_{dcB}}{2}-\frac{1}{3}\left(\frac{V_{dcB}}{\omega T_t}(T+F)-\frac{V_{dcB}}{2}\right)$	$\left(\frac{1}{\omega L}\right)\left(\frac{V_{dcA}-V_{dcB}}{\omega T_t}\frac{(\theta^2-(T+F+\varphi)^2)}{2}-\frac{V_{dcA}(T+F)-V_{dcB}(T+F+3\varphi)}{3\omega T_t}(\theta-T-F-\varphi)-\frac{V_{dcA}-V_{dcB}}{3}(\theta-T-F-\varphi)\right)+i_5$	$T+F+\varphi<\theta<\omega T_t$

TABLE VII
ARM ENERGY VARIATION IN EO MODE

Sr. No	$e^{EO}(\theta)$	Time period
1	$e_{u1}^{EO}(\theta)=\left(\frac{1}{\omega L}\right)\left(-\frac{3V_{dcA}^2-V_{dcA}V_{dcB}}{36(\omega T_t)^3}\theta^5+\frac{V_{dcA}^2F+V_{dcA}V_{dcB}(T+F-\varphi)}{12(\omega T_t)^3}\theta^4+\frac{(V_{dcA}^2-2V_{dcA}V_{dcB})}{12(\omega T_t)^2}\theta^4\right)-V_{dcA}i_0\frac{\theta^3}{3(\omega T_t)^2}+\left(\frac{1}{\omega L}\right)\left(\frac{3V_{dcA}^2-V_{dcA}V_{dcB}}{12(\omega T_t)^2}\frac{\theta^4}{2}-\frac{V_{dcA}^2F+V_{dcA}V_{dcB}(T+F-\varphi)}{9(\omega T_t)^2}\theta^3-\frac{(V_{dcA}^2-2V_{dcA}V_{dcB})}{9\omega T_t}\theta^3\right)+V_{dcA}i_0\frac{\theta^2}{2\omega T_t}$	$0<\theta<\varphi$
2	$e_{u2}^{EO}(\theta)=\left(\frac{1}{\omega L}\right)\left(-\frac{V_{dcA}^2-V_{dcA}V_{dcB}}{(\omega T_t)^3}\frac{(\theta^5-\varphi^5)/5-\varphi^2(\theta^3-\varphi^3)/3}{2}+\frac{V_{dcA}^2F-V_{dcA}V_{dcB}(F+3\phi)}{3(\omega T_t)^3}((\theta^4-\varphi^4)/4-\phi(\theta^3-\varphi^3)/3)+\frac{(V_{dcA}^2-V_{dcA}V_{dcB})}{3(\omega T_t)^2}((\theta^4-\varphi^4)/4-\phi(\theta^3-\varphi^3)/3)\right)-V_{dcA}i_1\frac{(\theta^3-\varphi^3)/3}{(\omega T_t)^2}+\left(\frac{1}{\omega L}\right)\left(\frac{V_{dcA}^2-V_{dcA}V_{dcB}}{(\omega T_t)^2}\frac{(\theta^4-\varphi^4)/4-\varphi^2(\theta^2-\varphi^2)/2}{2}-\frac{V_{dcA}^2F-V_{dcA}V_{dcB}(F+3\phi)}{3(\omega T_t)^2}((\theta^3-\varphi^3)/3-\phi(\theta^2-\varphi^2)/2)-\frac{(V_{dcA}^2-V_{dcA}V_{dcB})}{3(\omega T_t)}((\theta^3-\varphi^3)/3-\phi(\theta^2-\varphi^2)/2)\right)+V_{dcA}i_1\frac{(\theta^2-\varphi^2)/2}{\omega T_t}$	$\varphi<\theta<F$
3	$e_{u3}^{EO}(\theta)=\left(\frac{1}{\omega L}\right)\left(-\frac{2/3V_{dcA}^2-V_{dcA}V_{dcB}}{(\omega T_t)^3}\frac{(\theta^5-F^5)/5-F^2(\theta^3-F^3)/3)}{2}-\frac{V_{dcA}V_{dcB}}{3(\omega T_t)^3}(F+3\varphi)((\theta^4-F^4)/4-F(\theta^3-F^3)/3)+\frac{V_{dcA}^2-V_{dcA}V_{dcB}}{3(\omega T_t)^2}((\theta^4-F^4)/4-F(\theta^3-F^3)/3)\right)-V_{dcA}i_2\frac{(\theta^3-F^3)/3}{(\omega T_t)^2}+\left(\frac{1}{\omega L}\right)\left(\frac{2/3V_{dcA}^2-V_{dcA}V_{dcB}}{(\omega T_t)^2}\frac{((\theta^4-F^4)/4-F^2(\theta^2-F^2)/2)}{2}+\frac{V_{dcA}V_{dcB}}{3(\omega T_t)^2}(F+3\varphi)((\theta^3-F^3)/3-F(\theta^2-F^2)/2)-\frac{V_{dcA}^2-V_{dcA}V_{dcB}}{3(\omega T_t)}((\theta^3-F^3)/3-F(\theta^2-F^2)/2)\right)+V_{dcA}i_2\frac{(\theta^2-F^2)/2}{\omega T_t}$	$F<\theta<F+\varphi$
4	$e_{u4}^{EO}=\left(\frac{1}{\omega L}\right)\left(-\frac{2}{3}\frac{V_{dcA}^2-V_{dcA}V_{dcB}}{(\omega T_t)^3}\frac{((\theta^5-(F+\varphi)^5)/5-(F+\varphi)^2(\theta^3-(F+\varphi)^3)/3)}{2}-\frac{2}{3}\frac{V_{dcA}V_{dcB}}{(\omega T_t)^3}\varphi((\theta^4-(F+\varphi)^4)/4-(F+\varphi)(\theta^3-(F+\varphi)^3)/3)+\frac{V_{dcA}^2-V_{dcA}V_{dcB}}{3(\omega T_t)^2}((\theta^4-(F+\varphi)^4)/4-(F+\varphi)(\theta^3-(F+\varphi)^3)/3)\right)-V_{dcA}i_3\frac{(\theta^3-(F+\varphi)^3)/3}{(\omega T_t)^2}+\left(\frac{1}{\omega L}\right)\left(\frac{2}{3}\frac{V_{dcA}^2-V_{dcA}V_{dcB}}{(\omega T_t)^2}\frac{((\theta^4-(F+\varphi)^4)/4-(F+\varphi)^2(\theta^2-(F+\varphi)^2)/2)}{2}+\frac{2}{3}\frac{V_{dcA}V_{dcB}}{(\omega T_t)^2}\varphi((\theta^3-(F+\varphi)^3)/3-(F+\varphi)(\theta^2-(F+\varphi)^2)/2)-\frac{V_{dcA}^2-V_{dcA}V_{dcB}}{3\omega T_t}((\theta^3-(F+\varphi)^3)/3-(F+\varphi)(\theta^2-(F+\varphi)^2)/2)\right)+V_{dcA}i_3\frac{(\theta^2-(F+\varphi)^2)/2}{\omega T_t}$	$F+\varphi<\theta<T+F$
5	$e_{u5}^{EO}=\left(\frac{1}{\omega L}\right)\left(-\frac{V_{dcA}^2-\frac{2}{3V_{dcA}V_{dcB}}}{(\omega T_t)^3}\frac{((\theta^5-(F+T)^5)/5-(T+F)^2(\theta^3-(F+T)^3)/3)}{2}+\frac{V_{dcA}^2(T+F)-V_{dcA}V_{dcB}(2\varphi)}{3(\omega T_t)^3}((\theta^4-(F+T)^4)/4-(T+F)(\theta^3-(F+T)^3)/3)+\frac{V_{dcA}^2-V_{dcA}V_{dcB}}{3(\omega T_t)^2}((\theta^4-(F+T)^4)/4-(T+F)(\theta^3-(F+T)^3)/3)\right)-V_{dcA}i_4\frac{(\theta^3-(F+T)^3)/3}{(\omega T_t)^2}+\left(\frac{1}{\omega L}\right)\left(\frac{V_{dcA}^2-2/3V_{dcA}V_{dcB}}{(\omega T_t)^2}\frac{((\theta^4-(F+T)^4)/4-(T+F)^2(\theta^2-(F+T)^2)/2)}{2}-\frac{V_{dcA}^2(T+F)-V_{dcA}V_{dcB}(2\varphi)}{3(\omega T_t)^2}((\theta^3-(F+T)^3)/3-(T+F)(\theta^2-(F+T)^2)/2)-\frac{V_{dcA}^2-V_{dcA}V_{dcB}}{3(\omega T_t)}((\theta^3-(F+T)^3)/3-(T+F)(\theta^2-(F+T)^2)/2)\right)+V_{dcA}i_4\frac{(\theta^2-(F+T)^2)/2}{\omega T_t}$	$T+F<\theta<T+F+\varphi$
6	$e_{u6}^{EO}=\left(\frac{1}{\omega L}\right)\left(-\frac{V_{dcA}^2-V_{dcA}V_{dcB}}{(\omega T_t)^3}\frac{((\theta^5-(F+T+\varphi)^5)/5-(T+F+\varphi)^2(\theta^3-(F+T+\varphi)^3)/3)}{2}+\frac{V_{dcA}^2(T+F)-V_{dcA}V_{dcB}(T+F+3\varphi)}{3(\omega T_t)^3}((\theta^4-(F+T+\varphi)^4)/4-(T+F+\varphi)(\theta^3-(F+T+\varphi)^3)/3)+\frac{V_{dcA}^2-V_{dcA}V_{dcB}}{3(\omega T_t)^2}((\theta^4-(F+T+\varphi)^4)/4-(T+F+\varphi)(\theta^3-(F+T+\varphi)^3)/3)\right)-V_{dcA}i_5\frac{(\theta^3-(F+T+\varphi)^3)/3}{(\omega T_t)^2}+\left(\frac{1}{\omega L}\right)\left(\frac{V_{dcA}^2-V_{dcA}V_{dcB}}{(\omega T_t)^2}\frac{((\theta^4-(F+T+\varphi)^4)/4-(T+F+\varphi)^2(\theta^2-(F+T+\varphi)^2)/2)}{2}-\frac{V_{dcA}^2(T+F)-V_{dcA}V_{dcB}(T+F+3\varphi)}{3(\omega T_t)^2}((\theta^3-(F+T+\varphi)^3)/3-(T+F+\varphi)(\theta^2-(F+T+\varphi)^2)/2)-\frac{V_{dcA}^2-V_{dcA}V_{dcB}}{3\omega T_t}((\theta^3-(F+T+\varphi)^3)/3-(T+F+\varphi)(\theta^2-(F+T+\varphi)^2)/2)\right)+V_{dcA}i_5\frac{(\theta^2-(F+T+\varphi)^2)/2}{\omega T_t}$	$T+F+\varphi<\theta<\omega T_t$

ACKNOWLEDGMENT

This publication is a joint outcome of the R&D work undertaken in the project under grants TETRA TTR/2021/000048 and CRG CRG/2018/000926 schemes by Science and Engineering Board (SERB), Government of India

REFERENCES

[1] M. P. Bahrman and B. K. Johnson, "The ABCs of HVdc transmission technologies," *IEEE Power Energy Mag.*, vol. 5, no. 2, pp. 32–44, Mar./Apr. 2007.
[2] CIGRE WG B4.52, "Feasibility of HVdc grids," CIGRE tec. Brochure 533, Paris, France, Apr. 2013.
[3] D. Jovcic et al., "DC-DC converters in HVdc grids and for connections to HVdc systems," CIGRE, Paris, France, Tech. Rep. WG. B4.76, Mar. 2021.
[4] Y. Chen, S. Zhao, Z. Li, X. Wei, and Y. Kang, "Modeling and control of the isolated DC–DC modular multilevel converter for electric ship medium voltage direct current power system," *IEEE J. Emerg. Sel. Topics Power Electron.*, vol. 5, no. 1, pp. 124–139, Mar. 2017.
[5] G. Zheng, Y. Chen, and Y. Kang, "Trapezoidal current modulation for a compact DC modular multilevel converter with ZVS of submodules and ZCS of voltage-balancing circuits," *IEEE Trans. Power Electron.*, vol. 36, no. 10, pp. 10986–10992, Oct. 2021.
[6] J. D. Páez, D. Frey, J. Maneiro, S. Bacha, and P. Dworakowski, "Overview of DC–DC converters dedicated to HVdc grids," *IEEE Trans. Power Del.*, vol. 34, no. 1, pp. 119–128, Feb. 2019.
[7] R. Feldman et al., "A hybrid modular multilevel voltage source converter for HVdc power transmission," *IEEE Trans. Ind. Appl.*, vol. 49, no. 4, pp. 1577–1588, Jul./Aug. 2013.
[8] B. Zhao, Q. Song, J. Li, Y. Wang, and W. Liu, "High-frequency-link modulation methodology of DC–DC transformer based on modular multilevel converter for HVdc application: Comprehensive analysis and experimental verification," *IEEE Trans. Power Electron.*, vol. 32, no. 5, pp. 3413–3424, May 2017.
[9] G. A. Reddy and A. Shukla, "Circulating current optimization control of MMC," *IEEE Trans. Ind. Electron.*, vol. 68, no. 4, pp. 2798–2811, Apr. 2021.
[10] S. Debnath, J. Qin, B. Bahrani, M. Saeedifard, and P. Barbosa, "Operation, control, and applications of the modular multilevel converter: A review," *IEEE Trans. Power Electron.*, vol. 30, no. 1, pp. 37–53, Jan. 2015.
[11] M. S. Ansari, A. Shukla, and H. J. Bahirat, "Modeling of MMC based high power DC-DC converter controlled using trapezoidal modulation," in *Proc. IEEE Energy Convers. Congr. Expo.*, 2020, pp. 5716–5722.
[12] A. Mertens and J. Kucka, "Quasi two-level PWM operation of an MMC phase leg with reduced module capacitance," *IEEE Trans. Power Electron.*, vol. 31, no. 10, pp. 6765–6769, Oct. 2016.
[13] I. A. Gowaid, G. P. Adam, A. M. Massoud, S. Ahmed, D. Holliday, and B. W. Williams, "Quasi two-level operation of modular multilevel converter for use in a high-power DC transformer with DC fault isolation capability," *IEEE Trans. Power Electron.*, vol. 30, no. 1, pp. 108–123, Jan. 2015.
[14] I. A. Gowaid, G. P. Adam, A. M. Massoud, S. Ahmed, and B. W. Williams, "Hybrid and modular multilevel converter designs for isolated HVdc–DC converters," *IEEE J. Emerg. Sel. Topics Power Electron.*, vol. 6, no. 1, pp. 188–202, Mar. 2018.
[15] C. Sun, J. Zhang, Y. Chang, G. Shi, and X. Cai, "Wide voltage range operation of isolated modular multilevel DC-DC converter," in *Proc. Ind. Electron., Control, Instrum. Conf.—41st Annu. Conf. IEEE Ind. Electron. Soc.*, 2015, pp. 004953–004958.
[16] C. Sun, X. Cai, J. Zhang, and G. Shi, "Suppression of reactive power in isolated modular multilevel DC–DC converter under quasi square-wave modulation," *IEEE Access*, vol. 7, pp. 23940–23950, 2019.
[17] M. A. Elgenedy, A. Darwish, S. Ahmed, and B. W. Williams, "A transition arm modular multilevel universal pulse-waveform generator for electroporation applications," *IEEE Trans. Power Electron.*, vol. 32, no. 12, pp. 8979–8991, Dec. 2017.
[18] Y. Qiao, X. Zhang, X. Xiang, X. Yang, and T. C. Green, "Trapezoidal current modulation for bidirectional high-step-ratio modular DC–DC converters," *IEEE Trans. Power Electron.*, vol. 35, no. 4, pp. 3402–3415, Apr. 2020.
[19] P. Li, G. P. Adam, S. J. Finney, and D. Holliday, "Operation analysis of thyristor-based front-to-front active-forced-commutated bridge DC transformer in LCC and VSC hybrid HVdc networks," *IEEE J. Emerg. Sel. Topics Power Electron.*, vol. 5, no. 4, pp. 1657–1669, Dec. 2017.
[20] M. B. Ghat, A. Shukla, and R. Mishra, "Variable slope trapezoidal reference signal based control for a DC fault tolerant hybrid modular multilevel converter with cascaded full bridges," *IEEE Trans. Ind. Appl.*, vol. 53, no. 4, pp. 3770–3781, Jul./Aug. 2017.
[21] M. M. C. Merlin et al., "The alternate arm converter: A new hybrid multilevel converter with DC-fault blocking capability," *IEEE Trans. Power Del.*, vol. 29, no. 1, pp. 310–317, Feb. 2014.
[22] M. M. C. Merlin and T. C. Green, "Cell capacitor sizing in multilevel converters: Cases of the modular multilevel converter and alternate arm converter," *IET Power Electron.*, vol. 8, no. 3, pp. 350–360, 2015.

Mohd Shadab Ansari (Student Member, IEEE) received the B.Tech. degree in electrical engineering from the University College of Engineering, Kota, India, in 2015. Since 2016, he has been working toward the M.Tech.-Ph.D. dual degree in electrical engineering with the Indian Institute of Technology Bombay, Mumbai, India.

His research interests include power electronic converters for HVdc applications, high power dc–dc converters, and multilevel converters.

Anshuman Shukla (Senior Member, IEEE) received the M.Tech. and Ph.D. degrees in electrical engineering from Indian Institute of Technology Kanpur, Kanpur, India, in 2003 and 2008, respectively.

From 2008 to 2011, he was a Scientist with ABB Corporate Research Center, Västerås, Sweden. In 2008, he was a Research Associate with the Department of Electrical Engineering, University of South Carolina, Columbia, SC, USA. In 2011, he joined Indian Institute of Technology Bombay, Mumbai, India, where he is currently a Professor with the Department of Electrical Engineering. His research interests include multilevel converters, power electronics for HVdc, MVdc, and FACTS applications, grid-connected systems, dc–dc converters, solid-state transformers, motor drives, and the application of silicon carbide power electronics.

Dr. Shukla was a recipient of the 2021 Technology Translation Award conferred by SERB, Government of India, the 2011 Young Engineer Award conferred by the Institution of Engineers, India, and the MeiTy Visveswaraya Young Faculty Research Fellowship for the term 2018–2023. He is currently an Associate Editor for the IEEE JOURNAL OF EMERGING AND SELECTED TOPICS IN POWER ELECTRONICS.

Himanshu J. Bahirat (Senior Member, IEEE) received the B.E. degree in electrical engineering from the Visvesvaraya Regional College of Engineering, Nagpur, Nagpur, India, in 2002, and the M.S.E.E. and Ph.D. degrees in electrical engineering from Michigan Technological University, Houghton, MI, USA, in 2009 and 2013, respectively.

He was with Schneider Electric Private Ltd. and Larsen & Toubro Ltd. at their design centers in India, working in the area of circuit-breaker design. He is currently a Faculty with the Department of Electrical Engineering, Indian Institute of Technology Bombay, Mumbai, India.